# Contactless and Spatially Resolved Determination of Current–Voltage Curves in Perovskite Solar Cells via Photoluminescence

*Anh Dinh Bui,\* Md Arafat Mahmud, Naeimeh Mozaffari, Rabin Basnet, The Duong, Gabriel Bartholazzi, Tien T. Le, Thien N. Truong, Mike Tebyetekerwa, Ary Wibowo, Klaus J. Weber, Thomas P. White, Kylie R. Catchpole, Daniel Macdonald,\* and Hieu T. Nguyen\**

Early prediction of spatially resolved performance of perovskite solar cells (PSCs) is essential for process monitoring, control and fault diagnosis, and upscaling of this emerging technology. Herein, a fast, nonde structive, contactless imaging-based approach is developed to visualize the spatial distribution of possible light current density–voltage (pseudo-$J$–$V$) curves on finished and partly finished cells. This allows for the extraction of other critical spatially resolved properties including implied open-circuit voltage and pseudo-fill factor. The technique is applied to systematically investigate various degradation behaviors on PSCs including thermal stability, light soaking, and ambient air exposure. Finally, it is used to predict pseudo-$J$–$V$ curves of various perovskite films with different compositions. These results demonstrate the significant value of this fast imaging technique for the research and development of PSCs ranging from material selection, process optimization, to degradation study.

## 1. Introduction

Since it was first demonstrated with a power conversion efficiency (PCE) of 4% in 2009,[1] perovskite solar cells (PSCs) have rapidly improved in both efficiency (reaching 25.5% PCE[2]) and stability (passing standard International Electrotechnical Commission tests for certain cell architectures and perovskite compositions).[3] Therefore, this low-cost technology is a very

A. D. Bui, N. Mozaffari, Dr. R. Basnet, Dr. T. Duong, G. Bartholazzi, T. T. Le, T. N. Truong, M. Tebyetekerwa, A. Wibowo, Prof. K. J. Weber, Prof. T. P. White, Prof. K. R. Catchpole, Prof. D. Macdonald, Dr. H. T. Nguyen
School of Engineering
The Australian National University
Canberra, ACT 2601, Australia
E-mail: anh.bui@anu.edu.au; daniel.macdonald@anu.edu.au; hieu.nguyen@anu.edu.au

Dr. M. A. Mahmud
School of Physics
The University of Sydney
Sydney, NSW 2006, Australia

The ORCID identification number(s) for the author(s) of this article can be found under https://doi.org/10.1002/solr.202100348.

promising candidate for next-generation solar cells. Nevertheless, there are still many challenges to be solved to realize the successful commercialization of this technology. First, the PCE of PSCs still needs to be improved at both cell and module levels, when compared with the established crystalline silicon (c-Si) technology.[4] Second, a majority of perovskite compositions and cell architectures reported suffer from significant degradation caused by various factors including moisture, temperature, light exposure, and electrical bias.[5–9] The degradation is even more severe under real operating conditions as these factors often occur concurrently. Furthermore, despite the demonstrated high efficiency at the cell level ($25.5 \pm 0.8\%$, $0.0954\,\mathrm{cm}^2$),[10,11] the record module efficiency is still just 17.9% for an $802\,\mathrm{cm}^2$ area by Panasonic, which is significantly lower than that of c-Si solar modules.[2] To overcome these challenges, a lot of effort has been undertaken to improve the cell performance and durability by tuning perovskite compositions[12–14] or utilizing different passivation layers,[15–18] transport layers, electrodes, [19–21] and encapsulation methods.[22–24] Besides that, the requirement of reliable, fast, and nondestructive methods for full-size spatially monitoring material qualities and rapidly detecting defects and degradation in PSCs becomes increasingly significant.

Currently, the most straightforward way to quantify the performance of finished PSCs is to capture their light current density–voltage ($J$–$V$) characteristic curves using a solar simulator. From the $J$–$V$ curves, the efficiency and other crucial electrical parameters for evaluating the cell quality and durability including short-circuit current density ($J_{sc}$), open-circuit voltage ($V_{oc}$), fill factor (FF), hysteresis effects, and short- and long-term stability can be extracted.[25,26] However, this approach requires a complete device and electrical contacts; thus, it is impossible to quantify performance of partly finished cells at intermediate processing steps. In addition, the $J$–$V$ curves obtained from a solar simulator provide global information only; hence, they cannot be used to pinpoint
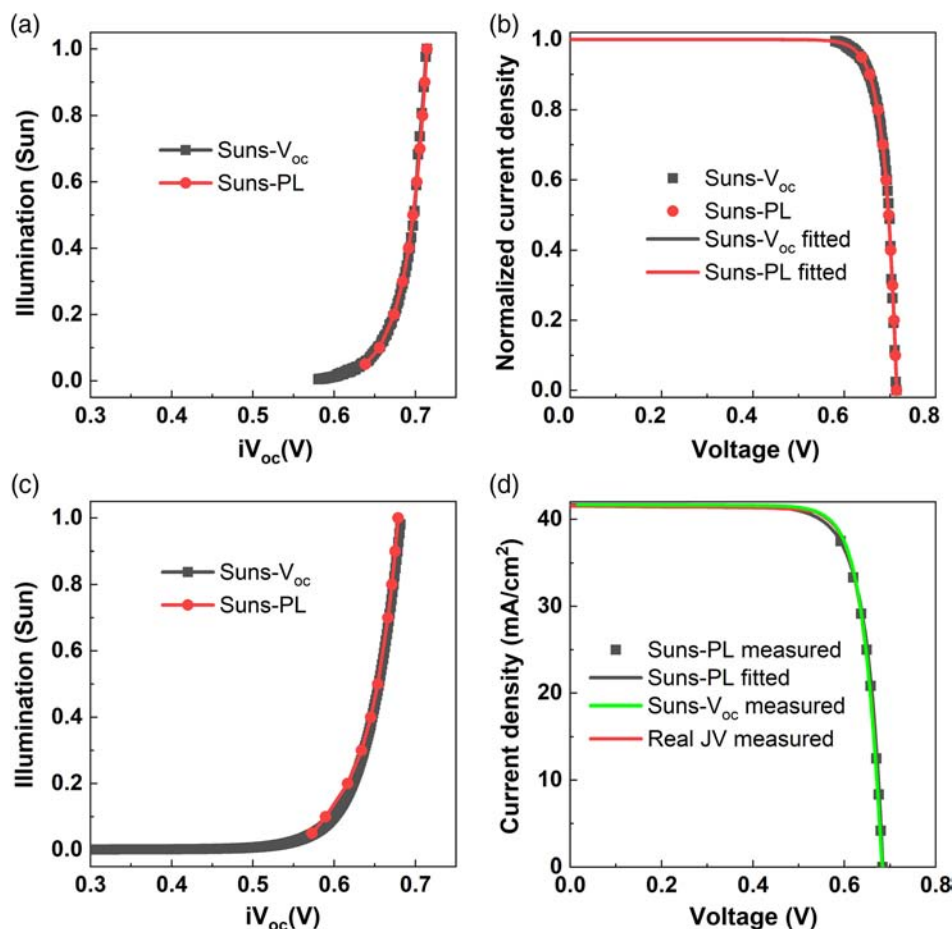
**Figure 1.** a,c) Suns$-V_{oc}$ (white-light class C spectrum) and Suns$-$PL (excitation wavelength of 808 nm) curves of (a) a double-side AlO$_x$-passivated c-Si wafer and (c) a finished c-Si solar cell. b,d) Pseudo-$J-V$ curves, converted from Suns$-V_{oc}$ and Suns$-$PL measurements of (b) the wafer (normalized current density $= 1-$Sun) and (d) the solar cell (current density $J = J_{sc} \times (1-$Sun$)$, where $J_{sc}$ is the short-circuit current density at 1$-$Sun illumination). The real $J-V$ data are also included in (d) for the solar cell.

the exact location of problems (for example, defects or degraded regions). Quantification of the spatial distribution of the key cell parameters during device fabrication and afterward becomes increasingly critical in predicting ultimate device performance and tracking process homogeneity.[27]

Photoluminescence (PL) imaging is a mainstream characterization technique for Si photovoltaics (PV) due to its many advantages compared with other techniques: it is fast, nondestructive, contactless, and has good spatial resolution.[28–33] Most significantly, photons captured in PL measurements are the result of the recombination of free electrons (in the conduction band) and holes (in the valence band), which contribute directly to the device current and voltage. Therefore, PL is one of the most direct measurements of material quality and device performance. It can be applied to various fabrication steps with high spatial resolution.[31,32,34–36] Among numerous PL-based applications reported, Suns-PL is an established technique to quantify possible light current density–voltage (pseudo-$J-V$) curves of c-Si solar cells, without the influence of series resistance, by simultaneously measuring implied open-circuit voltages ($iV_{oc}$) of finished or partly finished cells and incident light intensities.[32,33,35–37] The pseudo-$J-V$ curve is then used to extract

the cell's possible FF (pseudo-FF), shunt resistance ($R_{sh}$), and saturation current densities. The key point of this method is to convert the integrated PL intensity into $iV_{oc}$ at different incident light intensities. The Suns$-iV_{oc}$ curve can then be converted into the pseudo-$J-V$ curve under 1-sun illumination using a superposition principle, as reported by Sinton and Cuevas.[38] Recently, this method has been demonstrated on PSCs,[39] where pseudo-$J-V$ curves are constructed by investigating the dependence of quasi-Fermi-level splitting (equivalent to $iV_{oc}$) on illumination intensity. However, this work reports the global pseudo-$J-V$ curves only, which does not really take full advantage of the spatial information. Besides that, luminescence imaging has also attracted some attention from the perovskite community recently, reporting various applications such as quasi-Fermi-level splitting,[39–41] optical bandgap,[42] series resistance,[43] and various degradation behaviors.[44–46] However, its presence in perovskite research is still modest.

In this work, we report applications of Suns-PL imaging to determine spatially resolved information of electrical parameters across different perovskite films and PSCs in a contactless and nondestructive mode. First, we briefly explain the underlying mechanisms of the Suns-PL imaging method,
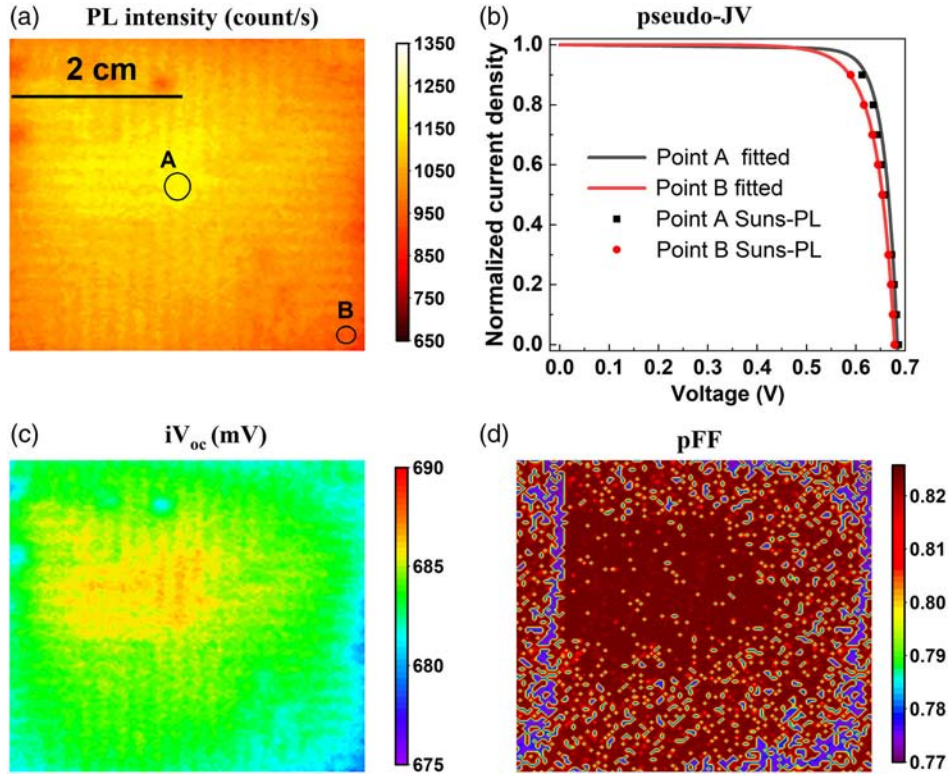
**Figure 2.** a) PL intensity image, b) pseudo-$J$−$V$ curves at the highest (point A) and lowest (point B) PL locations, c) $iV_{oc}$ image, and d) pseudo-FF image of the c-Si solar cell.

tailored to our experimental setups. We then verify the method on well-passivated c-Si wafers and complete solar cells. After that, we demonstrate the method to determine spatially resolved pseudo-$J$−$V$ curves on PSCs, allowing us to extract images of $iV_{oc}$ and pseudo-FF. We also use the imaging method to observe degradation processes of PSCs under various conditions including air exposure, temperature, and light soaking. Finally, this method is applied to predict the performance of various perovskite films with varying compositions.

## 2. Method Descriptions

In this section, we describe the procedure to convert detected intensities at each pixel ($I_{xy\_detected}$) of a standard PL image into each individual pseudo-$J$−$V$ curves. According to the generalized Planck's law, the PL spectrum emitted from an excited semiconductor sample is given by Equation (1).[47–49]

$$PL_{emitted}(E) = C \times A(E) \times E^2 \times \exp\left(\frac{-E}{kT}\right) \times \exp\left(\frac{\Delta\mu}{kT}\right) \quad (1)$$

where $A(E)$ is the energy-dependent absorptivity of the sample, $k$ is Boltzmann's constant, and $T$ is the sample's absolute temperature. $\Delta\mu$ is the quasi-Fermi-level splitting of electron–hole pairs, which is equivalent to $iV_{oc}$ ($iV_{oc} = \Delta\mu/q$, $q$ is an elemental charge) of the excited sample, and $C$ is a physical constant. In a PL imaging system, only a fraction of emitted photons can be collected by its objective lens. Also, these collected photons pass through different optical components before reaching the detector. Therefore, the detected intensity at each pixel is an energy-dependent integration of the product of the emitted spectrum, the collected fraction (scaling factor SF), and the spectral response (SR) of the entire system. It is given by

$$I_{xy\_detected} = SF \times \int_{E_1}^{E_2} \left[ C \times SR(E) \times A(E) \times E^2 \right.$$
$$\left. \times \exp\left(\frac{-E}{kT}\right) \times \exp\left(\frac{iV_{OC}}{V_T}\right) \right] dE \quad (2)$$

Here, $V_T = kT/q$ is the thermal voltage. $E_1$ and $E_2$ are the lower and upper limits of the energy interval containing the full PL spectrum. The scaling factor SF and SR are fixed for a certain experimental setup. The former can be determined using a high-quality calibration solar cell with known values of $V_{oc}$ (see Supporting Information), whereas the latter can be measured for all optical components using a spectrophotometer. As SF and $iV_{oc}$ are energy independent, Equation (2) can be rearranged as

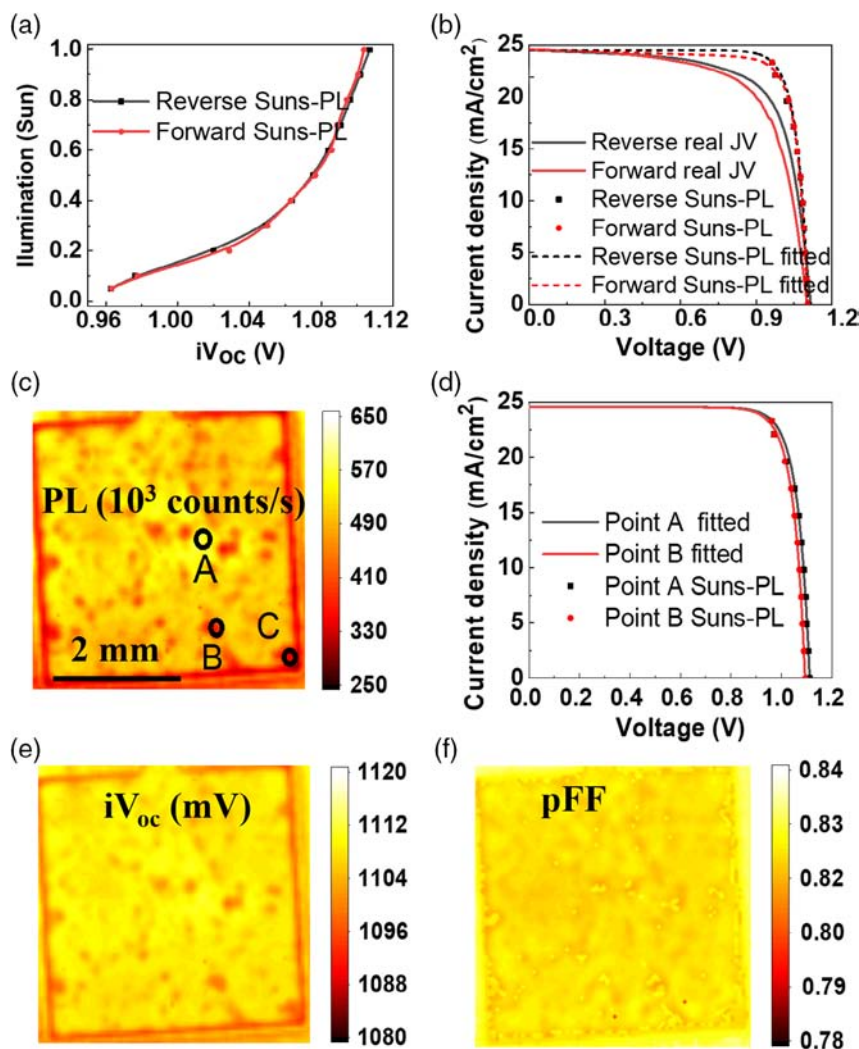$$iV_{OC} = V_T \times \ln\left(\frac{I_{xy\_detected}}{B \times SF}\right) \quad (3)$$

**Figure 3.** a) Suns−PL curve of a working PSC. b) Extracted pseudo-$J$−$V$ and real $J$−$V$ curves of the cell under 1-Sun illumination. c) PL intensity image (under 1-Sun illumination, excitation wavelength of 430 nm). d) Pseudo-$J$−$V$ curves at good PL (point A) and low-PL signal locations (point B). e) $iV_{oc}$ image. f) Pseudo-FF image.

where

$$B = \int_{E_1}^{E_2} C \times \text{SR}(E) \times A(E) \times E^2 \times \exp\left(\frac{-E}{kT}\right) dE \qquad (4)$$

Therefore, by varying illumination intensities and capturing the corresponding PL intensity images, Suns−$iV_{oc}$ curves (i.e., $iV_{oc}$ vs illumination intensity) can be constructed for each pixel and then converted to pseudo-$J$−$V$ curves using a superposition principle, as reported by Sinton and Cuevas.[38] From these curves, pseudo-FFs can be spatially resolved, giving useful information about recombination pathways and predicting early local lifetimes of absorbers, as reported by Michl et al.[50]

A critical assumption in the procedure is that the absorptivity $A(E)$ around the luminescence peak is uniform across a sample. We conducted microabsorptivity mapping across several locations within PSCs before and after degradation tests and found them

relatively uniform at different wavelengths around the luminescence peak (Figure S1 and S2, Supporting Information). Therefore, this assumption is valid for our investigated samples. Furthermore, if surface defects exist, the concentrations of holes and electrons can vary depth wise, leading to a change in $\Delta\mu$ or $iV_{oc}$. Therefore, the $iV_{oc}$ value determined from this method is considered as an average value across the sample thickness. Another important assumption is that contacts are ideal for good quality cells, reducing mismatches between external $V_{oc}$ and $iV_{oc}$. In this case, we can measure the external $V_{oc}$ of a working solar cell and use this value to calibrate the SF of any luminescence imaging system.[51] Also, two different imaging systems are used to validate the method. For Si cells and wafers, we use a commercial BT imaging system with an excitation wavelength of 808 nm and a charge-coupled device (CCD) Si camera. For perovskite cells and films, we use a homebuilt imaging system with an excitation wavelength of 430 nm and a similar Si camera.
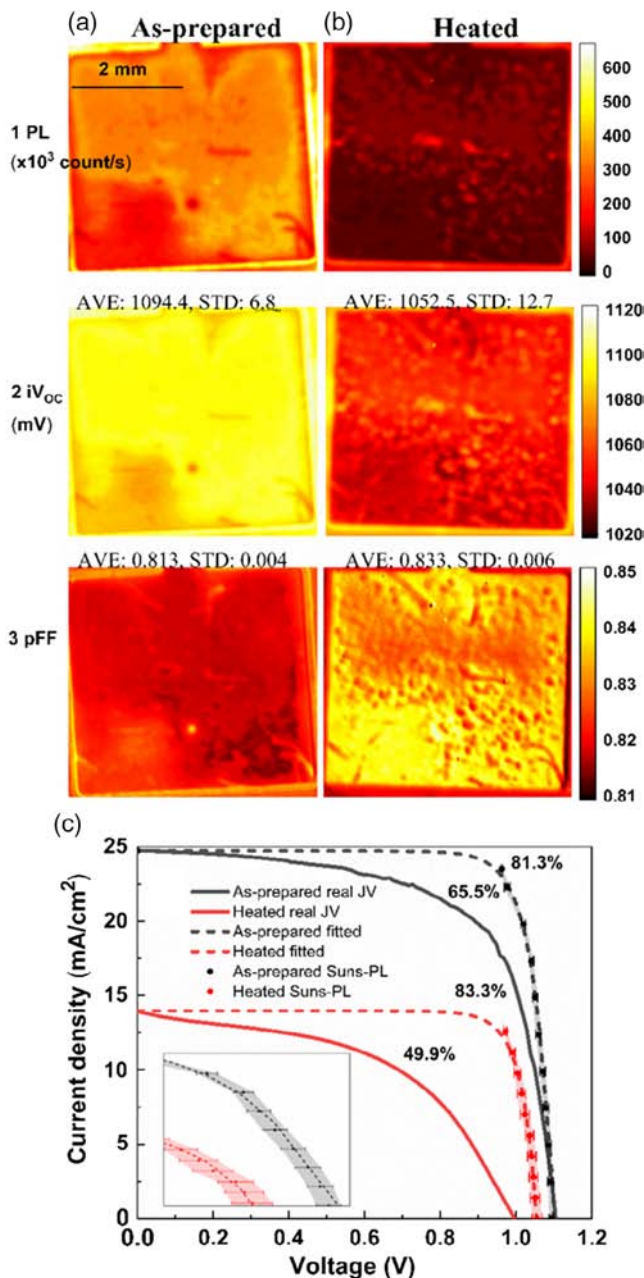
**Figure 4.** a,b) (1) PL intensity (under 1-Sun illumination, excitation wavelength of 430 nm), (2) $iV_{oc}$, (3) pseudo-FF images, and (c) extracted pseudo-$J-V$ curve versus real $J-V$ curve of a working PSC before and after heating at 90 °C in 30 min (inset: shaded region representing one standard deviation of $iV_{oc}$ across the cell). Columns a and b correspond to before and after the heat test, respectively.

# 3. Results and Discussions

## 3.1. Validation on c-Si Wafers and Solar Cells

First, we validate our setup and calibration procedure on a well-passivated c-Si wafer and high-quality c-Si solar cell. For the c-Si wafer (**Figure 1**a,b), we compare our results with Suns−$iV_{oc}$ data obtained from the well-established quasisteady-state photoconductance (QSSPC) method.[51,52] For the high-quality c-Si solar cell (PCE > 22%) (Figure 1c,d), we compare our results with both Suns−$V_{oc}$ and real $J−V$ curves under a $J−V$ tester. The global Suns−PL curve is the average of the entire sample under test. In Figure 1, the $V_{oc}$ versus illumination intensity (a,c) and $J−V$ (b,d) data show an excellent agreement among the three methods (Suns−PL, Suns−$V_{oc}$, and real $J−V$ measurements), validating our setup and procedure. Moreover, due to the limitation of our PL tool sensitivity, we here carry out the Suns−PL measurements down to 0.05 Sun only and then fit the results with a simplified double-diode model to reconstruct the complete pseudo-$J−V$ curves. The fit Suns−PL and Suns−$V_{oc}$ pseudo-$J−V$ curves are nearly identical, confirming the validity of this approach (for example, see Figure 1b). The FF obtained from the pseudo-$J$-$V$ curve is usually larger than that obtained from the real $J−V$ curve, as the former is not affected by series resistance. However, in Figure 1d, they are very similar, ≈81%, demonstrating a very low series resistance value of the solar cell.

The biggest advantage of the Suns-PL imaging method, compared with the Suns-$V_{oc}$ method and real $J−V$ data, is the ability to extract spatial information of the sample (courtesy of the imaging tool), from which one can quickly pinpoint problematic regions. In our work, at each pixel in a PL intensity image, we can construct an individual pseudo-$J−V$ curve to evaluate its electrical quality. **Figure 2** shows a spatial view of the c-Si solar cell in terms of aggregate PL intensity (2a), $iV_{oc}$ (2c), and pseudo-FF (2 d). Similar information from the c-Si wafer can be found in Figure S3, Supporting Information. The corresponding pseudo-$J−V$ curves of the best and worst locations are also shown in Figure 2b. From Figure 2c, the $iV_{oc}$ distribution of this cell is relatively uniform at 683.7 ± 1.27 mV. However, near the cell edges (location B), the $iV_{oc}$ and pseudo-FF are lower than the center (location A), attributed to a higher recombination activity around the edges. These spatial results cannot be obtained with the Suns-$V_{oc}$ method and real $J−V$ data.

## 3.2. Applications on PSCs

Now, we extend the Suns-PL imaging method to PSCs. **Figure 3**a shows a global $iV_{oc}$ versus illumination intensity curve of a working PSC, averaged across its active area, for both forward and reverse biases. Meanwhile, Figure 3b compares its extracted global pseudo-$J−V$ and real $J−V$ curves. In this case, the pseudo-FF from the Suns−PL curve is much higher than that from the real $J−V$ curve (82% vs 75%), consistent with data reported in the literature.[39] In Figure 3b, as the $V_{oc}$ is similar, the reduction in FF is mainly attributed to parasitic resistances. Hereafter, to simplify the presentation, we show data for reverse scans only.

Figure 3c,e,f show images of PL intensity, $iV_{oc}$, and pseudo-FF of the cell, respectively. We find that even good PSCs often show very nonuniform PL intensities and $iV_{oc}$ values. Various points with reduced PL intensities in the solar cell (dark regions in Figure 3c,e) can be observed. They could be due to the incorporation of impurities during solution preparation or unreacted $PbI_2$ causing I-rich regions.[42] Therefore, their pseudo-$J−V$ curves are highly location dependent, as shown in Figure 3d for various regions across the PSC. Around the cell edges (for
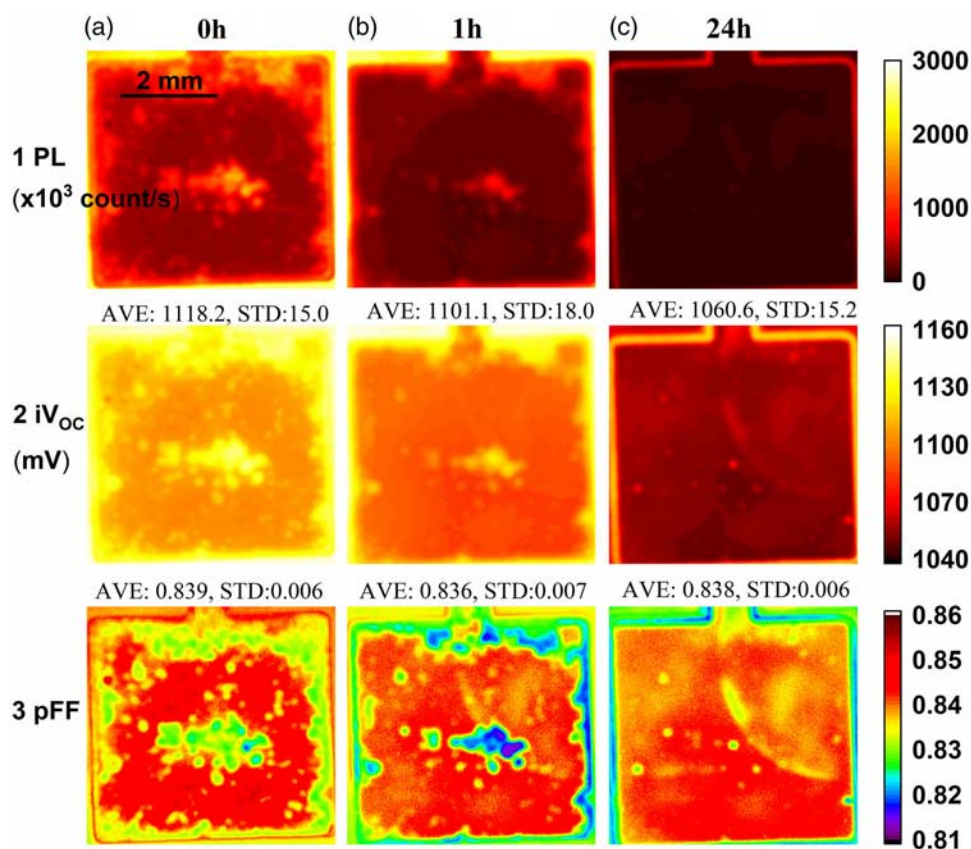
**Figure 5.** a–c) (1) PL intensity (under 1-Sun illumination, excitation wavelength of 430 nm), (2) $iV_{oc}$, and (3) pseudo-FF images of a PSC versus exposure time in air. Columns (a−c) correspond to different exposure times.

example, location C), the pseudo-$J−V$ curves are generally worse than those inside the cell (location A). Also, even inside the cell, there are still local regions with lower performance (location B), which may be caused by higher defect densities or impurities.[42] The $iV_{oc}$ difference between these regions is up to 20 mV.

Next, we demonstrate the applications of the Suns-PL imaging technique to monitor PSCs' local electrical parameters after various degradation tests. First, we conduct a temperature stability test by heating a finished PSC to 90 °C in 30 min. The cell electrical parameters before and after the test are shown in **Figure 4**. The average PL intensity (4.1a vs 4.1b) significantly decreases by one order of magnitude, which is equivalent to ≈50 mV in $iV_{oc}$ (4.2a vs 4.2b), across the PSC. Surprisingly, pseudo-FF values slightly increase after heating (4.3a vs 4.3b). The reason behind this phenomenon could be a feature of resistance-limited lateral balancing current. After the degradation test, the fraction of the low-lifetime region increases, leading to a reduced effect of lateral current and hence an increased pseudo-FF, as reported by Michl et al.[50]

Due to the sensitivity of pseudo-FF with shunt resistances created by pinholes in perovskite absorbers,[27] imaging the FF of perovskite-based devices can, in principle, provide useful spatial information on the quality of the absorbers, hence an indication for further optimization of the fabrication process. In addition, as the FF and ideality factor are interchangeable parameters (i.e., from ideality factor and $iV_{oc}$, we can calculate pseudo-FF or

FF under different measurement conditions[53]), spatially resolving these pieces of information (p-FF, $iV_{oc}$) concurrently is useful for the investigation of recombination mechanisms, limiting the performance of solar cells where degradation occurs differently location wise.[54] Furthermore, by combining with pervious works on series resistance imaging,[43] the method could offer a full protocol to spatially quantify performance loss during and after the fabrication process.

Figure 4c compares the global real and pseudo-$J−V$ curves of the cell before and after heating. It can be seen that initially the $V_{oc}$ values from both measurements are equivalent, similar to the case in Figure 3b. The PL-based $V_{oc}$ ($iV_{oc}$) reflects mainly the absorber and passivation quality, whereas the real $V_{oc}$ (from the $J−V$ test) reflects the entire cell structure. Therefore, the results suggest that the cell has very good transport layers and interfaces. However, after heating, the $iV_{oc}$ reduces by ≈50 mV, whereas the real $V_{oc}$ reduces up to 150 mV. The $iV_{oc}$ reduction is obviously due to the degradation of the absorber and passivation. Meanwhile, the significant $V_{oc}$ loss between the two methods demonstrates that the transport layers and interfaces are also damaged. This also leads to a further reduction in the real FF (65.5% before heating to only 49.9% after heating) due to the increasing parasitic resistances. Therefore, combining both real and pseudo-$J−V$ data can assist the degradation investigation on PSCs. We also conduct a similar study on the effects
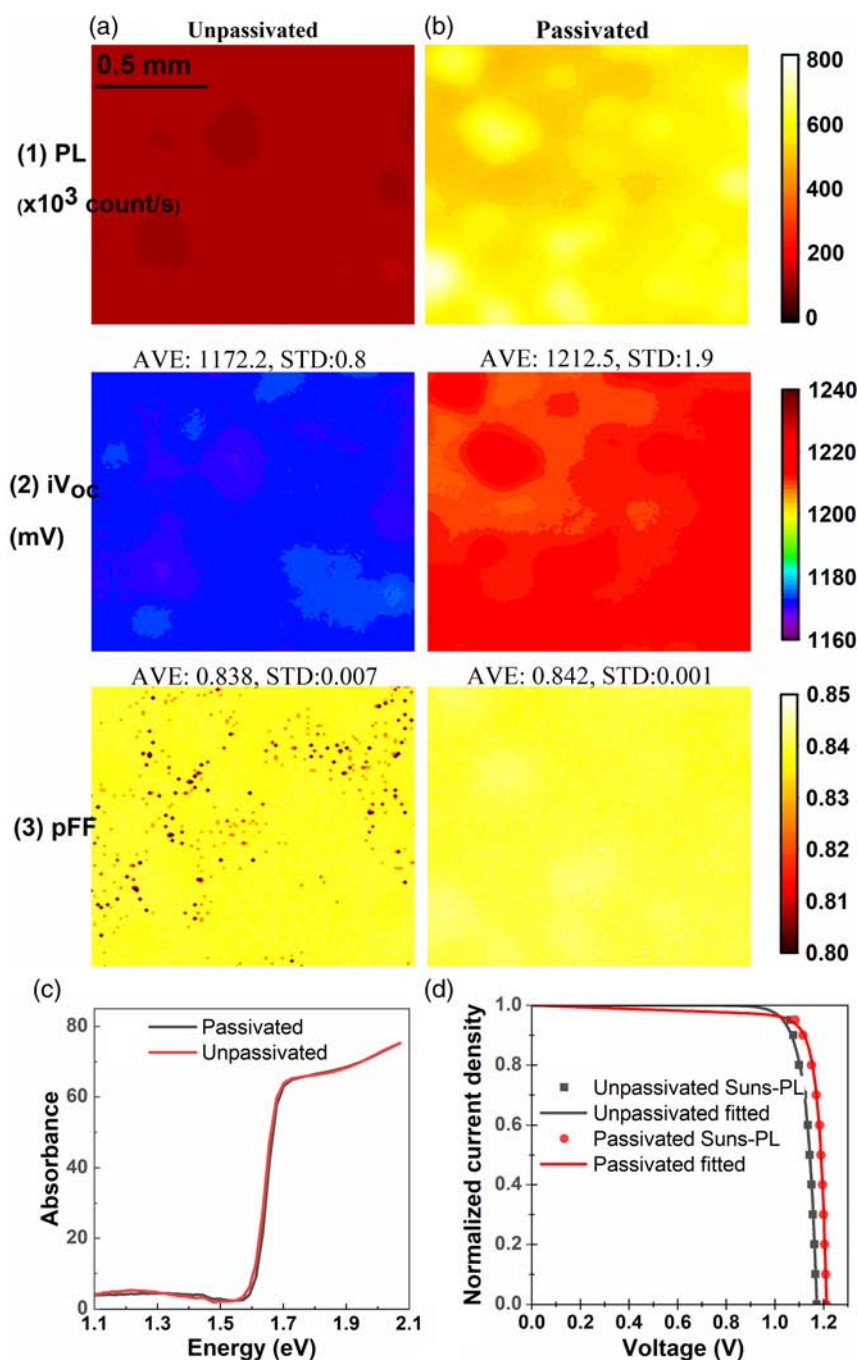
**Figure 6.** Images of PL intensity (row 1) (under 1 Sun illumination, excitation wavelength of 430 nm), $iV_{oc}$ (row 2), and pseudo-FF (row 3) of a quadruple cation $Cs_{0.07}Rb_{0.03}FA_{0.765}MA_{0.135}PbI_{2.55}Br_{0.45}$ perovskite film a) with and b) without a passivation layer. c) Absorptivity and d) pseudo-$J$−$V$ curves of the perovskite film with and without a passivation layer.

of light soaking on PSCs, in which the $iV_{oc}$ values of both the finished cell and perovskite film reduce by ≈60 mV, whereas the real $V_{oc}$ value extracted from the $J$−$V$ curve reduces by ≈150 mV, after the cell and film are exposed under 1-Sun illumination for 30 min without controlling the temperature (see Figure S4, Supporting Information). In addition, the distribution of $iV_{oc}$ is consistently broadened after all the degradation tests (see Table S1–S3, Supporting Information), which implies

different degradation effects at different parts of the cells. This effect can be seen clearly in the inset of Figure 4c. These observations would not be possible without the spatially resolved capability.

Next, **Figure 5** shows images of PL intensity (row 1), $iV_{oc}$ (row 2), pseudo-FF (row 3), and their evolutions with time of another PSC after it is exposed to air. The cell degrades significantly after 24 h in the air (≈100 mV drop in $iV_{oc}$). It should be noted that this PSC has
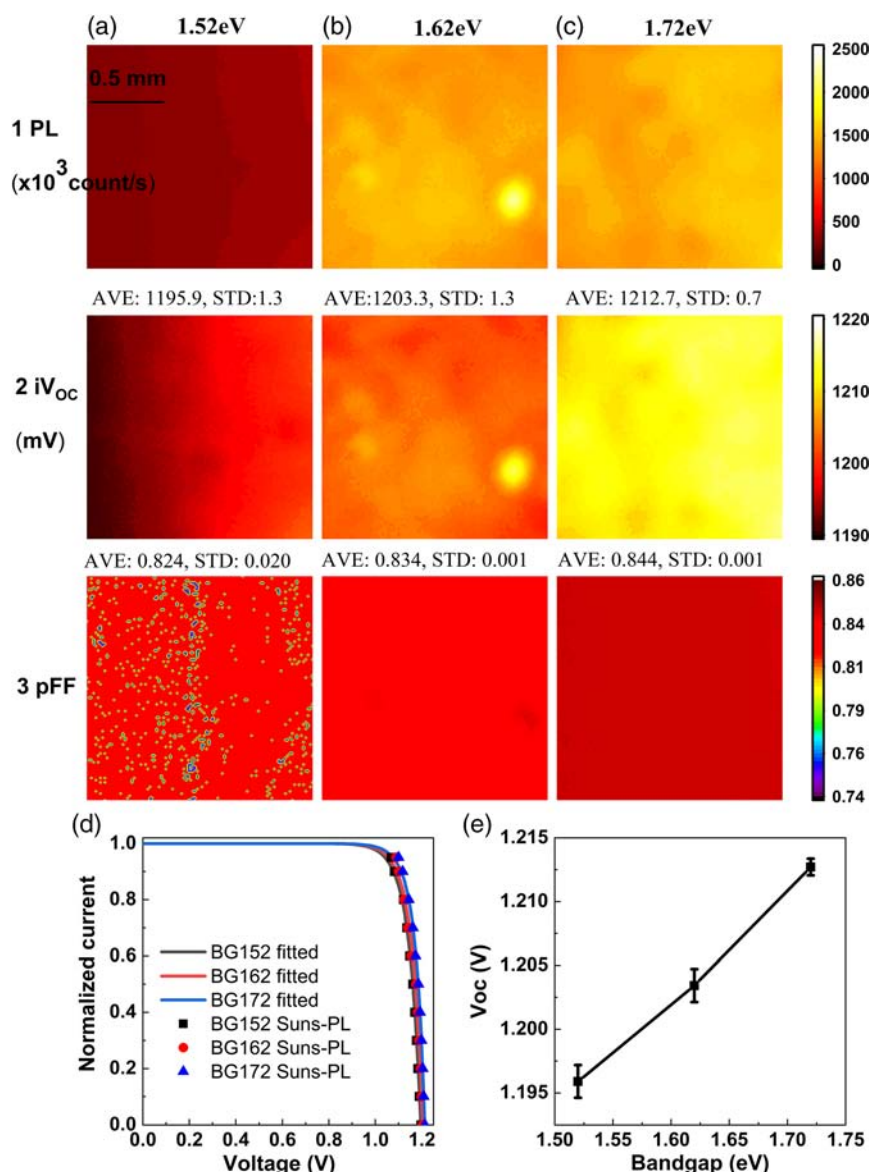
**Figure 7.** a–c) PL intensity (row 1) (under 1 Sun illumination, excitation wavelength of 430 nm), $iV_{oc}$ (row 2), and pseudo-FF (row 3) images of perovskite films with different bandgaps. Columns (a–c) correspond to different bandgap values. d) Global pseudo–$J$–$V$ curves and e) average $iV_{oc}$ versus bandgap of the films.

been stored in a desiccator for several days before the test. This could lead to some prior degradation, which is displayed through the highly nonuniform PL, $iV_{oc}$, or pseudo-FF images in the beginning. Also, the rate of degradation depends strongly on the cell architecture and quality. Therefore, the observation here should not be a generalization of all PSCs. Here, we emphasize on the applications of the Suns-PL imaging technique to provide spatially resolved information of critical electrical parameters to monitor the degradation, rather than its mechanism in PSCs.

### 3.3. Performance Prediction of Perovskite Films

Another major advantage of the Suns-PL imaging method is that it is conducted under a contactless mode. Therefore, it can be

applied directly on perovskite films or partially finished PSCs to predict possible $J$–$V$ curves or monitor the effects of fabrication processes on the cell performance. To demonstrate these capabilities, we first apply the method on a quadruple cation $Cs_{0.07}Rb_{0.03}FA_{0.765}MA_{0.135}PbI_{2.55}Br_{0.45}$ perovskite film with and without a passivation layer. **Figure 6** shows PL intensity (row 1), $iV_{oc}$ (row 2), and pseudo-FF (row 3) images of the film with and without the passivation layer. Although the absorptivity of both samples is identical (Figure 6c), a significant increase in PL intensity is observed (6.1a vs 6.1b), which leads to ≈40 mV improvement in $iV_{oc}$ (6.2a vs 6.2b or 6d for global pseudo-$J$–$V$ curves). The increases in PL intensity and $iV_{oc}$ can be attributed to a reduction of nonradiative recombination at the surface after passivation. In addition, the suppression of the nonradiative

surface recombination improves the pseudo-FF (6.3a vs 6.2b or 6d), which is similar to previous works of Stolterfoht et al.[39,41]

Furthermore, we systematically study possible $J-V$ curves of different films with varying bandgaps. By tuning precursor compositions, we get films with bandgap values of 1.52, 1.62, and 1.72 eV, which are determined by their absorption spectra (Figure S5, Supporting Information). **Figure 7**a–c shows their PL intensity (row 1), $iV_{oc}$ (row 2), and pseudo-FF (row 3) images. Their global possible $J-V$ curves and average $iV_{oc}$ are shown in Figure 7d,e, respectively. It is clear that higher-bandgap films yield higher $iV_{oc}$ and pseudo-FF values. However, with these perovskite films, a 200 meV increase in bandgap results in a modest 17 mV increase in $iV_{oc}$ and only 2% increase in pseudo-FF. A direct implication from these results is that there is no benefit in terms of $iV_{oc}$ and FF when fabricating complete solar cells with the highest-bandgap film at this stage. Therefore, one should focus on increasing the film quality first. Other cell fabrication optimizations should be done only after reasonable improvement in the film's possible $J-V$ curve. These applications demonstrate that Suns-PL imaging is a very powerful tool to predict and monitor the performance and heterogeneity of finished and unfinished PSCs even at the material level.

## 4. Conclusion

We have reported the applications of the Suns-PL imaging technique to spatially resolve possible $J-V$ curves of PSCs and films. The technique is fast, contactless, nondestructive, and it can be applied at various fabrication stages. The technique has been validated on c-Si solar cells and wafers and confirmed by other independent measurements. We then applied the technique to monitor $J-V$ curves and other electrical parameters of PSCs after various degradation tests, including air exposure, temperature, and light soaking. Observing these $J-V$ curves gives us some insights about the degradation behaviors on PSCs under different conditions. We have also further applied this method to predict potential performance of perovskite films with various compositions and with and without passivation layers. These preliminary applications open exciting opportunities for this imaging concept to be a quantified, high spatially resolved, large-area characterization tool of perovskite materials and devices. This could be significant for the study of various degradation mechanisms, morphology homogeneity, and reproducibility improvements, or process monitoring on large-area cells and precursors.

## 5. Experimental Section

Details of Experimental Section are provided in the Supporting Information.

## Supporting Information

Supporting Information is available from the Wiley Online Library or from the author.

## Conflict of Interest

The authors declare no conflict of interest.

## Author Contributions

H.T.N. conceived the idea, designed the overall experiments, and supervised the project. D.M. cosupervised the project. A.D.B. carried out all optical measurements and simulations. M.M.A., T.D., G.B.L.C., N.M., and R.B. prepared the samples. M.M.A., T.D., G.B.L.C., N.M., R.B., T.T.L., T.N.T., M.T., A.W., K.J.W., T.P.W., K.R.C., and D.M. contributed to the results analysis and interpretation. H.T.N. and A.D.B. analyzed the data and wrote the manuscript. All authors contributed to the discussion of the results and reviewed the manuscript.

## Data Availability Statement

Research data are not shared.

[1] A. Kojima, K. Teshima, Y. Shirai, T. Miyasaka, *J. Am. Chem. Soc.* **2009**, *131*, 6050.

[2] *NREL best research cell efficiencies*, https://www.nrel.gov/pv/cell-efficiency.html (accessed: January 2020).

[3] L. Shi, M. P. Bucknall, T. L. Young, M. Zhang, L. Hu, J. Bing, D. S. Lee, J. Kim, T. Wu, N. Takamure, D. R. McKenzie, S. Huang, M. A. Green, A. W. Y. Ho-Baillie, *Science* **2020**, *368*, 1328

[4] C. Ma, N. Park, *Chem* **2020**, *6*, 1254.

[5] D. Di Girolamo, N. Phung, F. U. Kosasih, F. Di Giacomo, F. Matteocci, J. A. Smith, M. A. Flatken, H. Köbler, S. H. Turren Cruz, A. Mattoni, L. Cinà, B. Rech, A. Latini, G. Divitini, C. Ducati, A. Di Carlo, D. Dini, A. Abate, *Adv. Energy Mater.* **2020**, *10*, 2000310.

[6] J. A. Christians, P. A. Miranda Herrera, P. V. Kamat, *J. Am. Chem. Soc.* **2015**, *137*, 1530.

[7] W. Li, J. Fan, Y. Mai, L. Wang, *Adv. Energy Mater.* **2017**, *7*, 1701144.

[8] N. Aristidou, I. Sanchez-Molina, T. Chotchuangchutchaval, M. Brown, L. Martinez, T. Rath, S. A. Haque, *Angew. Chem., Int. Ed.* **2015**, *54*, 8208.

[9] S. Huang, Z. Li, L. Kong, N. Zhu, A. Shan, L. Li, *J. Am. Chem. Soc.* **2016**, *138*, 5749.

[10] M. Jeong, I. W. Choi, E. M. Go, Y. Cho, M. Kim, B. Lee, S. Jeong, Y. Jo, H. W. Choi, J. Lee, J. H. Bae, S. K. Kwak, D. S. Kim, C. Yang, *Science* **2020**, *369*, 1615.

[11] M. Green, E. Dunlop, J. Hohl-Ebinger, M. Yoshita, N. Kopidakis, X. Hao, *Prog. Photovoltaics Res. Appl.* **2021**, *29*, 3.

[12] Q. A. Akkerman, V. D'Innocenzo, S. Accornero, A. Scarpellini, A. Petrozza, M. Prato, L. Manna, *J. Am. Chem. Soc.* **2015**, *137*, 10276.

[13] Y. Zhou, Y. H. Jia, H. H. Fang, M. A. Loi, F. Y. Xie, L. Gong, M. C. Qin, X. H. Lu, C. P. Wong, N. Zhao, *Adv. Funct. Mater.* **2018**, *28*, 1803130.

[14] Y. Cai, L. Xie, Z. Zhang, Y. Zhou, H. Liu, X. Lu, X. Gao, J. Gao, L. Shui, S. Wu, J. Liu, *Electrochim. Acta* **2019**, *293*, 371.

[15] X. Liu, Z. Yu, T. Wang, K. L. Chiu, F. Lin, H. Gong, L. Ding, Y. Cheng, *Adv. Energy Mater.* **2020**, *10*, 2001958.

[16] C. Zhang, S. Wu, L. Tao, G. M. Arumugam, C. Liu, Z. Wang, S. Zhu, Y. Yang, J. Lin, X. Liu, R. E. I. Schropp, Y. Mai, *Adv. Energy Mater.* **2020**, *10*, 2002004.

[17] N. F. Ramli, P. N. A. Fahsyar, N. A. Ludin, M. A. M. Teridi, M. A. Ibrahim, S. Sepeai, *Mater. Chem. Phys.* **2021**, *257*, 123798.

[18] M. A. Mahmud, T. Duong, Y. Yin, H. T. Pham, D. Walter, J. Peng, Y. Wu, L. Li, H. Shen, N. Wu, N. Mozaffari, G. Andersson, K. R. Catchpole, K. J. Weber, T. P. White, *Adv. Funct. Mater.* **2020**, *30*, 1907962.

[19] T. Duong, H. K. Mulmudi, H. Shen, Y. L. Wu, C. Barugkin, Y. O. Mayon, H. T. Nguyen, D. Macdonald, J. Peng, M. Lockrey, W. Li, Y. B. Cheng, T. P. White, K. Weber, K. Catchpole, *Nano Energy* **2016**, *30*, 330.

[20] J. Peng, T. Duong, X. Zhou, H. Shen, Y. Wu, H. K. Mulmudi, Y. Wan, D. Zhong, J. Li, T. Tsuzuki, K. J. Weber, K. R. Catchpole, T. P. White, *Adv. Energy Mater.* **2017**, *7*, 1601768.

[21] T. Duong, J. Peng, D. Walter, J. Xiang, H. Shen, D. Chugh, M. Lockrey, D. Zhong, J. Li, K. Weber, T. P. White, K. R. Catchpole, *ACS Energy Lett.* **2018**, *3*, 2441.

[22] Z. Fu, M. Xu, Y. Sheng, Z. Yan, J. Meng, C. Tong, D. Li, Z. Wan, Y. Ming, A. Mei, Y. Hu, Y. Rong, H. Han, *Adv. Funct. Mater.* **2019**, *29*, 1809129.

[23] R. Cheacharoen, N. Rolston, D. Harwood, K. A. Bush, R. H. Dauskardt, M. D. McGehee, *Energy Environ. Sci.* **2018**, *11*, 144.

[24] F. Matteocci, L. Cinà, E. Lamanna, S. Cacovich, G. Divitini, P. A. Midgley, C. Ducati, A. Di Carlo, *Nano Energy* **2016**, *30*, 162.

[25] S. Bae, S. Kim, S. W. Lee, K. J. Cho, S. Park, S. Lee, Y. Kang, H. S. Lee, D. Kim, *J. Phys. Chem. Lett.* **2016**, *7*, 3091.

[26] H. J. Snaith, A. Abate, J. M. Ball, G. E. Eperon, T. Leijtens, N. K. Noel, S. D. Stranks, J. T. W. Wang, K. Wojciechowski, W. Zhang, *J. Phys. Chem. Lett.* **2014**, *5*, 1511.

[27] M. C. Schubert, L. E. Mundt, D. Walter, A. Fell, S. W. Glunz, *Adv. Energy Mater.* **2020**, *10*, 2004001.

[28] T. Trupke, R. A. Bardos, M. D. Abbott, J. E. Cotter, *Appl. Phys. Lett.* **2005**, *87*, 093506.

[29] B. Mitchell, J. W. Weber, M. Juhl, D. Macdonald, T. Trupke, *Solid State Phenom.* **2014**, *118*, 205.

[30] B. Hallam, Y. Augarten, B. Tjahjono, T. Trupke, S. Wenham, *J. Appl. Phys.* **2014**, *115*, 4862957.

[31] T. Trupke, R. A. Bardos, M. C. Schubert, W. Warta, *Appl. Phys. Lett.* **2006**, *89*, 044107.

[32] A. Delamarre, L. Lombez, J. F. Guillemoles, *Appl. Phys. Lett.* **2012**, *100*, 131108.

[33] Z. Hameiri, P. Chaturvedi, *Appl. Phys. Lett.* **2013**, *102*, 073502.

[34] T. Trupke, B. Mitchell, J. W. Weber, W. McMillan, R. A. Bardos, R. Kroeze, *Energy Procedia* **2012**, *15*, 135.

[35] J. Liu, A. Melnikov, A. Mandelis, *J. Appl. Phys.* **2013**, *114*, 4821120.

[36] R. Bhoopathy, O. Kunz, M. Juhl, T. Trupke, Z. Hameiri, *Prog. Photovoltaics Res. Appl.* **2018**, *26*, 69.

[37] V. Shanmugam, T. Mueller, A. G. Aberle, J. Wong, *Sol. Energy* **2015**, *118*, 20.

[38] R. A. Sinton, A. Cuevas, in *16th European Photovoltaic Solar Energy Conf.*, WIP-Renewable Energies, Glasgow **2000**, p. 1152.

[39] M. Stolterfoht, M. Grischek, P. Caprioglio, C. M. Wolff, E. Gutierrez-Partida, F. Peña-Camargo, D. Rothhardt, S. Zhang, M. Raoufi, J. Wolansky, M. Abdi-Jalebi, S. D. Stranks, S. Albrecht, T. Kirchartz, D. Neher, *Adv. Mater.* **2020**, *32*, 2000080.

[40] M. Stolterfoht, C. M. Wolff, J. A. Márquez, S. Zhang, C. J. Hages, D. Rothhardt, S. Albrecht, P. L. Burn, P. Meredith, T. Unold, D. Neher, *Nat. Energy* **2018**, *3*, 847.

[41] M. Stolterfoht, P. Caprioglio, C. M. Wolff, J. A. Márquez, J. Nordmann, S. Zhang, D. Rothhardt, U. Hörmann, Y. Amir, A. Redinger, L. Kegelmann, F. Zu, S. Albrecht, N. Koch, T. Kirchartz, M. Saliba, T. Unold, D. Neher, *Energy Environ. Sci.* **2019**, *12*, 2778.

[42] B. Chen, J. Peng, H. Shen, T. Duong, D. Walter, S. Johnston, M. M. Al-Jassim, K. J. Weber, T. P. White, K. R. Catchpole, D. Macdonald, H. T. Nguyen, *Adv. Energy Mater.* **2019**, *9*, 1802790.

[43] D. Walter, Y. Wu, T. Duong, J. Peng, L. Jiang, K. C. Fong, K. Weber, *Adv. Energy Mater.* **2018**, *8*, 1701522.

[44] A. M. Soufiani, M. J. Y. Tayebjee, S. Meyer, A. Ho-Baillie, J. Sung Yun, R. W. McQueen, L. Spiccia, M. A. Green, Z. Hameiri, *J. Appl. Phys.* **2016**, *120*, 4956436.

[45] M. Okano, M. Endo, A. Wakamiya, M. Yoshita, H. Akiyama, Y. Kanemitsu, *Appl. Phys. Express* **2015**, *8*, 102302.

[46] A. M. Soufiani, Z. Hameiri, S. Meyer, S. Lim, M. J. Y. Tayebjee, J. S. Yun, A. Ho-Baillie, G. J. Conibeer, L. Spiccia, M. A. Green, *Adv. Energy Mater.* **2017**, *7*, 1602111.

[47] P. Wurfel, *J. Phys. C Solid State Phys.* **1982**, *15*, 3967.

[48] E. Daub, P. Würfel, *Phys. Rev. Lett.* **1995**, *74*, 1020.

[49] G. El-Hajje, C. Momblona, L. Gil-Escrig, J. Ávila, T. Guillemot, J. F. Guillemoles, M. Sessolo, H. J. Bolink, L. Lombez, *Energy Environ. Sci.* **2016**, *9*, 2286.

[50] W. W. M. C. Schubert, B. Michl, D. Impera, M. Bivour, *Prog. Photovoltaics Res. Appl.* **2014**, *22*, 1114.

[51] R. A. Sinton, A. Cuevas, *Appl. Phys. Lett.* **1996**, *69*, 2510.

[52] R. A. Sinton, S. Consulting, S. Jose, A. Cuevas, M. Stuckings, *Proceedings of the 25th IEEE Photovoltaic Specialists Conference*, IEEE, Washington DC **1996**, 457.

[53] M. Leilaeioun, Z. C. Holman, *J. Appl. Phys.* **2016**, *120*, 123111.

[54] W. Tress, M. Yavari, K. Domanski, P. Yadav, B. Niesen, J. P. Correa Baena, A. Hagfeldt, M. Graetzel, *Energy Environ. Sci.* **2018**, *11*, 151.